Analysis and Enhanced Modeling of Inductive Displacement Sensor in Active Magnetic Bearing

Mohammad Ali Salahmanesh
Department of Electrical Engineering
Ferdowsi University of Mashhad
Mashhad, Iran
m.salahmanesh@mail.um.ac.ir

Salman Abdi Jalebi School of Engineering University of East Anglia Norwich, UK S.Abdi-Jalebi@uea.ac.uk Hossein Abootorabi Zarchi
Department of Electrical Engineering
Ferdowsi University of Mashhad
Mashhad, Iran
abootorabi@um.ac.ir

Gholamreza Arab Markadeh
Department of Electrical Engineering
Ferdowsi University of Mashhad
Mashhad, Iran
gh.arabmarkadeh@um.ac.ir

Hamidreza Mosaddegh-Hesar Department of Electrical Engineering University of Saskatchewan Saskatoon, Canada pvt356@mail.usask.ca

Ali Akbar Derakhshi
Kavosh Electronic Vanda Shargh
Mashhad, Iran
derakhshi@kevc.ir

Abstract— Inductive displacement sensors are commonly used in active magnetic bearing (AMB) applications. In most research, conventional models used to analyze inductive sensors in terms of determining sensitivity and obtaining a relationship between output voltage and displacement ignore the effects of fringing in air gaps. However, the effects of flux fringing on the performance of these sensors cannot be ignored in industrial applications. In this article, by using the Schwarz-Christoffel transformation, 3-D self- and mutual inductances for the radial and axial poles of a 3-degree-of-freedom inductive sensor are calculated, with the effects of fringing taken into account. The results of these calculations are compared with finite element results. The results show that the model based on the Schwarz-Christoffel method outperforms the ideal model in which flux fringing is ignored, with an inductance calculation error of about 8% for radial poles and 6.5% for axial poles, respectively.

Keywords—Schwarz-Christoffel transformation, Displacement sensor, Fringing effects, 3D inductances.

NOMENCLATURE

L_r Radial Inductance

La Axial Inductance

 D_{r1} Radial Pole Width (X-Y Plane)

 D_{r2} Radial Pole Width (Y-Z Plane)

 D_{a1} Axial Pole Width (X-Y Plane)

 D_{a2} Axial Pole Width (Y-Z Plane)

 H_r Radial Pole Height

H_a Axial Pole Height

H_t Rotor Target Height

Number of turns

 V_0 Horizontal line of constant potential in W-plane

 ψ Vertical line in W-plane

 μ_0 Relative Permeability

 ε_0 Permittivity of free space

I. INTRODUCTION

In the last three decades, active magnetic bearing (AMB) systems have been employed in various high-speed industrial applications due to their advantages, such as long life, absence of friction, and the elimination of the need for

lubrication systems [1]. One of the most crucial components of AMBs is the displacement sensors used in them, which play a pivotal role in the control system of AMBs. Currently, conventional displacement sensors used in magnetic bearing applications include inductive and eddy current sensors. While both sensors offer high sensitivity, eddy current sensors are sensitive to the material under test and entail a complex and expensive measurement system. These factors have contributed to a decrease in their utilization [2]. On the other hand, inductive sensors, owing to advantages such as a high signal-to-noise ratio, low cost, and long lifespan, represent a viable option for AMBs [3]. Consequently, extensive research has been conducted to enhance the design of these sensors, aiming to increase sensitivity, analyze working principles, and develop accurate models for inductive and self-inductive sensors.

In [4], a novel method is proposed for impedance modeling of self-inductive displacement sensors, particularly focusing on incorporating iron core reluctance and flux leakage considerations. This integration significantly enhances sensor accuracy and reliability, marking a notable advancement in displacement measurement techniques. A distinctive approach to radial displacement detection is presented in [5], where authors propose utilizing sensing coils weakly coupled with magnetic bearings. By leveraging this weak coupling, the sensor achieves exceptional precision and sensitivity, promising new possibilities for non-invasive displacement sensing in magnetic bearing systems. In the domain of angular displacement sensing, [6] introduces an absolute inductive sensor dedicated to position detection of YRT turntable bearings. This sensor facilitates accurate angular displacement measurement, thereby enabling precise positioning control in rotary motion systems. Ref. [7] contributes an integrated 5-degree-of-freedom (DOF) displacement sensor system designed for magnetically suspended flywheels. This system allows comprehensive monitoring of displacement in multiple directions, significantly enhancing the stability and performance of flywheel-based energy storage systems. The design and development of a new non-contact inductive displacement sensor is conducted in [8]. This sensor, known for its simplicity, reliability, and immunity to environmental conditions, is well-suited for diverse industrial applications requiring accurate displacement measurements. innovative approach to displacement self-sensing in active magnetic bearing (AMB) rotor systems is proposed in [9]. By employing current ripple demodulations combined with PWM command signals, this method enables accurate displacement sensing without additional sensors, simplifying AMB systems' control and monitoring. Investigating the effect of excitation signal on double-coil inductive displacement transducers, authors in [10] offer valuable insights into optimizing sensor design and performance for specific applications. An inductive sensor capable of twodimensional displacement measurement is proposed in [11]. This sensor design offers versatility and compactness for precise measurement of complex displacement patterns across various engineering systems. Ref. [12] delves into the structure design and simulation analysis of an inductive displacement Through simulation-based sensor. optimization, the authors enhance sensor sensitivity and accuracy, contributing to the development of highperformance sensor systems. An optimized differential selfinductance displacement sensor specifically designed for magnetic bearings is introduced in [13]. The sensor's effectiveness in accurately measuring displacement in magnetic bearing systems is demonstrated through comprehensive design, analysis, and experimentation, resulting in improved stability and performance. A robust three-dimensional position sensor for measuring rotor displacement in both radial and axial directions of an AMB system is proposed in [14], utilizing a unified sensor stator and inductive measuring principle. It demonstrates feasibility in a closed-loop control application with a high-speed industrial induction machine, offering an alternative solution to commercial eddy current displacement sensors while application requirements with meeting construction.

In most of the analyses concerning displacement sensors referenced above, the ideal model is typically employed. This model considers the reluctance of the air gap but disregards the effects of leakage, flux fringing, and the core reluctance. However, in many industrial applications, the dimensions of the magnetic poles of the sensor are often not significantly larger than the nominal air gap. Consequently, the leakage flux in the magnetic circuit increases as the air gap widens, adversely affecting sensor performance and introducing errors in the relationship between the sensor's output voltage and the rotor's displacement. Hence, there is a need to refine the ideal model to enhance accuracy. To address this, modeling techniques aimed at improving accuracy have been explored. These include measuring the complex permeability of the core in the magnetic position sensor using a B-H analyzer at different frequencies [15], incorporating the effect of flux leakage into the calculation of air gap reluctance [16-17], and considering the nonlinear effect of relative permeability. Additionally, analyses based on finite element model (FEM) often require significant computing time, and 3D FEM models tend to be complex.

Therefore, the main objective of this article is to account for the effects of flux leakage in air gaps by employing a theoretical model to calculate the matrix of inductances in the 3D geometry of a three DOF inductive sensor. Theoretical model results are compared with finite element results, demonstrating the superior accuracy of the theoretical model over the ideal one.

II. OPERATION PRINCIPLE OF 3-DOF INDUCTIVE SENSOR

The structure of the 3-DOF inductive Displacement sensor, shown in Fig. (1-a), is capable of measuring the radial and axial positions of the rotor, simultaneously. To measure the radial position, 4 single poles are used in each 90-degree area of the sensor circumference, and to measure the axial position, 4 double poles are used in the main horizontal and vertical directions of the sensor circle. The radial poles include two sets of wiring comprising two A and B axes of three DOF. To measure the radial position of the rotor in two axes, the same sinusoidal exciting circuit is used. When the rotor is moved from its central position under the effect of lateral forces, the length of the air gap in the magnetic circuit of a pair of radial poles of the sensor stator, which are shown in green or yellow in Fig. (1-a), changes. Therefore, by changing the length of the air gap, the reluctance of the air gap in this path will be modified and correspondingly, the self-inductance of the two-pole windings will change. As it can be seen in Figs. (1-b) and (1-c), The output feedback circuit for both axes are a bridge circuit. In the case that the

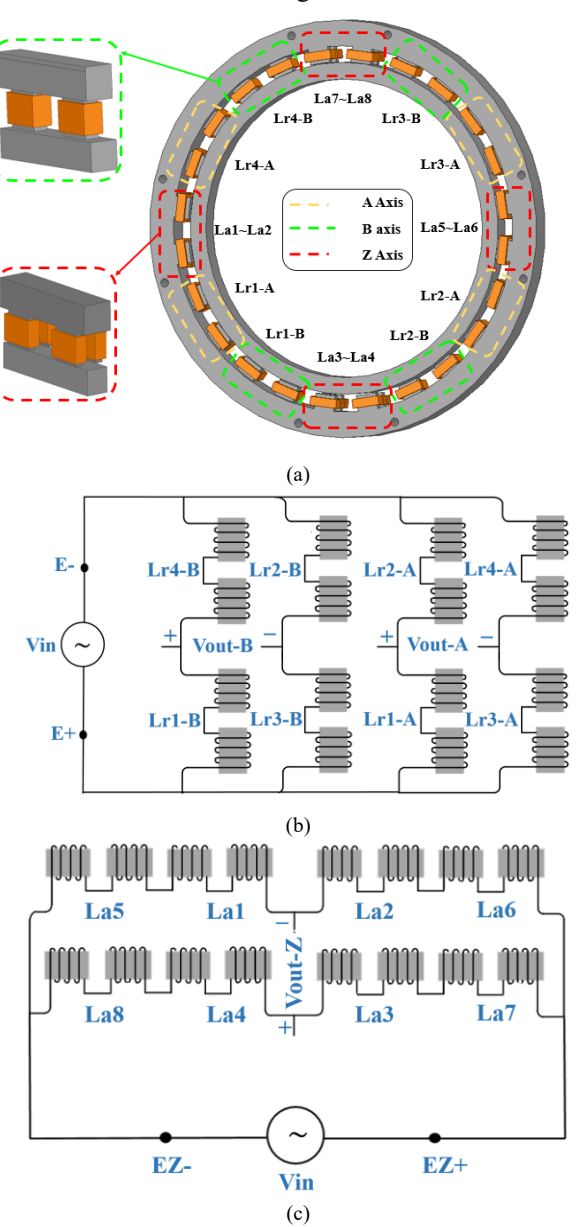


Fig. 1. (a) The structure of displacement sensor, (b) Radial poles wiring circuit, and (c) Axial poles wiring circuit

rotor is in its central position, $L_{r1-A} = L_{r2-A} = L_{r3-A} = L_{r4-A}$ and $L_{r1-B} = L_{r2-B} = L_{r3-B} = L_{r4-B}$, and therefore the output feedback voltage of both axes is zero. When the inductance is changed by varying the airgap length, the bridge circuit is out of balance and the voltage difference according to (1) is placed in its output:

$$V_{out-A} = \left(\frac{L_{r2-A}}{L_{r1-A} + L_{r2-A}} - \frac{L_{r4-A}}{L_{r3-A} + L_{r4-A}}\right) V_{in} \qquad (1)$$

$$V_{out-B} = \left(\frac{L_{r4-B}}{L_{r1-B} + L_{r4-B}} - \frac{L_{r2-B}}{L_{r3-A} + L_{r2-B}}\right) V_{in}$$
 (2)

The radial position of the rotor can be determined by the feedback voltage's amplitude and phase shift compared to the sinusoidal exciting voltage. When the rotor is moved axially, the measurement of this position of the shaft uses the same principles as the radial measurement, but in this case, the air gap reluctance changes based on the change of effective cross-section of the axial poles, instead of changing based on the radial air gap changes. In other words, when the ferromagnetic part of the rotor moves in the axial direction, the cross-section of two axial poles of the stator increases and the cross-section of others decreases. In the axial wiring circuit where the bridge circuit is used, the inductance of the facing poles in one axis is connected in series. This leads to the fact that when the shaft is moved radially, the inductance of each axial pole's winding changes, but the total inductance of the two windings does not change. As a result, the radial movement of the rotor will not affect the axial voltage feedback. The axial output voltage of the sensor is determined

$$V_{out-Z} = \begin{pmatrix} \frac{L_{a8} + L_{a4}}{L_{a3} + L_{a7} + L_{a8} + L_{a4}} \\ -\frac{L_{a1} + L_{a5}}{L_{a1} + L_{a2} + L_{a5} + L_{a6}} \end{pmatrix} V_{in}$$
(3)

At the axial balance point, where all the inductances L_{a1} to L_{a8} are equal together, the ferromagnetic part of the rotor overlaps with half of cross-section of each axial pole. Due to this axially located rotor position on the shaft, the elongation of the shaft can be determined by placing two sensors at the two ends of it. Finally, the radial and axial feedback voltages will be converted into a dc signal for each axis using the modulation circuit.

III. CALCULATION OF 3D INDUCTANCES OF RADIAL AND AXIAL POLES IN SENSOR RING

Based on the explanation provided in the previous section, the basic principles of this displacement sensor are based on the determination of the radial and axial pole inductances. Hence, the ideal model without considering fringing effects can be improved by calculating these inductances, accurately. In this section, the inductances of the radial and axial poles of the displacement sensor are determined using the analytical method based on the Schwarz-Christoffel transformation. Utilizing this transformation, an equation for the capacitance of a capacitor with an air dielectric can be derived, where the planes (conductor boundaries) have geometry and dimensions resembling those of the air gap of each radial and axial poles. To calculate the capacitance of this capacitor, the Schwarz-Christoffel transformation presented in (4) is used twice.

$$\frac{dz}{dt} = A(z_1 - u_1)^{(\theta_1/\pi) - 1} (z_1 - u_2)^{(\theta_2/\pi) - 1} \dots (z_1 - u_n)^{(\theta_n/\pi) - 1}$$
(4)

where $\theta_1, \theta_2, \theta_n$ are the interior angles of a polygon in the z plane, A is a constant parameter, and $u_1, u_2 \dots u_n$ are the coordinates of the points on the real axis of the z_1 plane corresponding to the corner points of the polygon in the z plane. In the first transformation, the air gap geometry under each radial and axial pole, which is considered as a polygon bounded by some straight lines, is transformed into the real axis of another plane (z_1) and the points inside this polygon are mapped to the points in the upper half of this real axis. In the second transformation, the two horizontal lines of capacitor plates in the W-plane are considered equivalent to the real axis of the z_1 plane. As a result, by using this real axis in the z_1 plane, the boundaries of the air gap's geometry in the z plane are transformed into the constant potential horizontal lines in the W plane. This transformation for air gap geometry under radial and axial poles is shown in Fig. (2). As it can be seen from this figure, a radial pole is divided into two equal parts in two x-y and y-z planes, and the transformation (4) is applied to only one of these halves, which is highlighted. In the end, once the capacitance is obtained for one half, the capacitance of entire radial pole will be obtained by parallelizing two capacitors with equal capacity. Considering the coordinates of two corner points of 2 and 4 where $u_1=0$, $u_2=1$, $\theta_1=0$ and $\theta_2=\frac{3\pi}{2}$, and placing them in (4), the transformation equation of z plane to z_1 plane for the radial pole is obtained as follows:

$$Z = -jA[2\ln(1+\sqrt{1-Z_1}) - \ln Z_1 - 2\sqrt{1-Z_1}] + B$$
 (5)

where the constant values of A and B are determined based on the boundary conditions $Z(Z_1=1)=0$ and $Z(Z_1\to 0)=\infty$ and are equal to $\frac{jg}{\pi}$ and zero, respectively. Again, using Schwarz-Christoffel transformation for Fig. (2-b) and corner point of $4(u_1=0)$. $\theta=0$ we have:

$$\frac{dW}{dz_1} = C(z_1 - 0)^{-1} = \frac{C}{z_1} . W = C \ln Z_1 + D$$
 (6)

where the constant values of C and D are determined based on the boundary conditions $W(z_1 = 1) = 0$ and $W(z_1 = -1) = jV_0$ and are equal to $\frac{V_0}{\pi}$ and zero, respectively. According to the capacitor shape in the W plane, the capacitance per unit length can be determined as follows:

$$C = \varepsilon_0 \frac{\psi_1 - \psi_3}{V_0} \tag{7}$$

According to the above analysis, the points of ψ_1 and ψ_3 inside the W plane are obtained as follows:

$$\psi_3 = \frac{-V_0}{\pi} \left(\frac{\pi D_{r1}}{2g} + 2(1 - \ln 2) \right) \cdot \psi_1 = \frac{2V_0}{\pi} \ln \left(\frac{\pi H_r}{2g} \right)$$
 (8)

As a result, (7) is rewritten for the radial half-pole structure as follows:

$$C = \varepsilon_0 \frac{\frac{2V_0}{\pi} \ln\left(\frac{\pi H_r}{2g}\right) + \frac{V_0}{\pi} \left(\frac{\pi D_{r1}}{2g} + 2(1 - \ln 2)\right)}{V_0}$$

$$= \varepsilon_0 \left[\frac{D_{r1}}{2g} + \frac{2}{\pi} \left(1 + \ln \frac{\pi H_r}{4g}\right)\right]$$
(9)

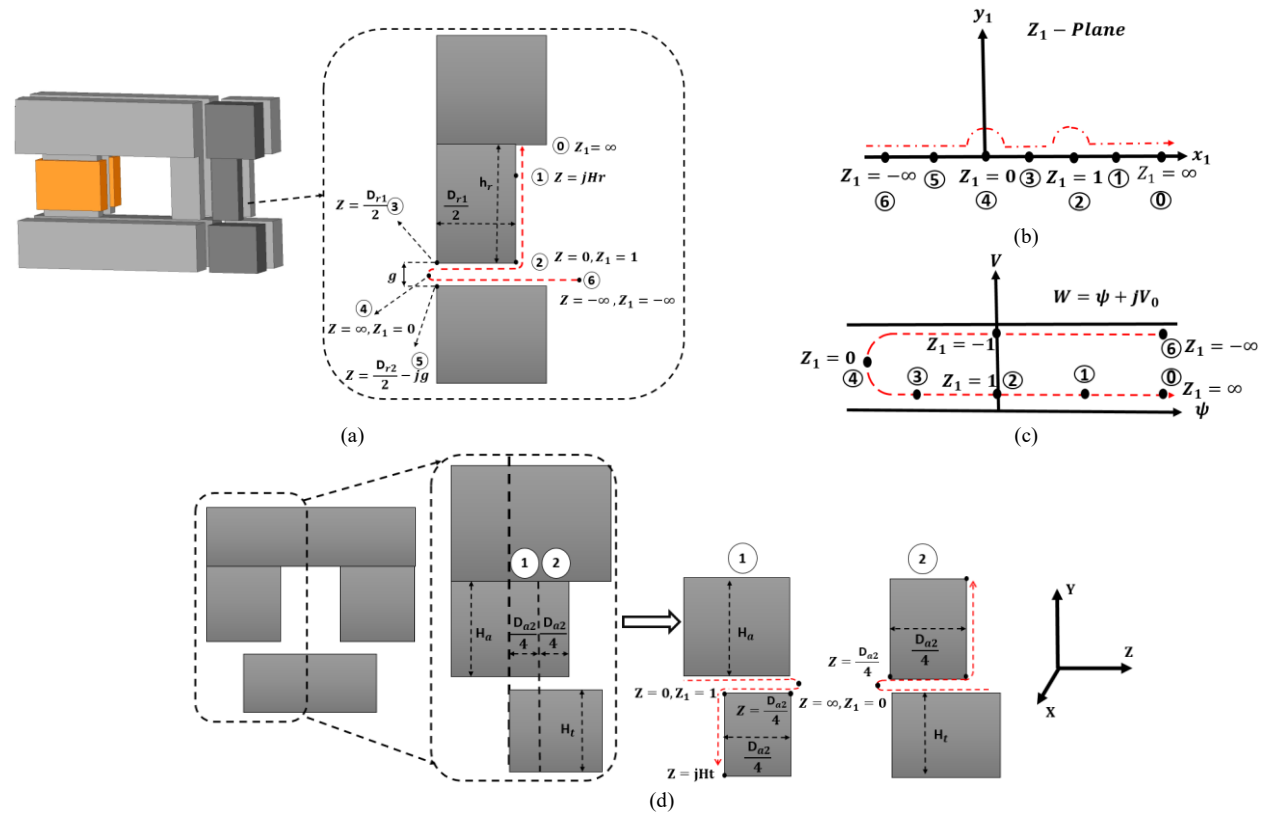


Fig. 2. (a) Radial airgap in x-y plane, (b) real axis in Z1 plane, (c) W plane, and (d) axial airgap in y-z plane

Equation (9) is similar for the other half of the radial pole. Generally, it can be said that the capacitance for a radial pole of the position sensor is obtained by parallelizing the capacitance of both halves. Now, by comparing the relationship between magnetic reluctance and capacitance, the reluctance of the air gap under a radial pole is determined as follows:

$$R_{r(x-y)} = \frac{1}{2\mu_0 \left[\frac{D_{r1}}{2g} + \frac{2}{\pi} \left(1 + \ln \frac{\pi H_r}{4g} \right) \right]}$$
(10)

Equation (10) is related to the air gap reluctance of radial poles in the x-y plane. In order to calculate inductances in three dimensions, it is required to determine reluctance in the y-z plane. In this plane, the reluctance relationship is the same as that of the x-y plane, except for the radial pole width is changed. Moreover, in each plane, the fringing factor can be obtained from the ratio of the calculated air gap reluctance per-unit-of-length to that of the ideal. Then, the 3D air gap reluctance can be obtained using (11) by multiplying the fringing factors of the two planes as outlined in (12).

$$R_{airgap} = \frac{\sigma_T g}{\mu_0 D_{r1} D_{r2}} \tag{11}$$

$$\sigma_T = \sigma_{x-y} \times \sigma_{y-z} \tag{12}$$

In the same way, the described procedure can be utilized to account for fringing effects in the air gap under axial poles. The capacitance for the axial pole in the x-y plane resembles that of the radial pole in this plane. However, the geometry of the axial pole in the y-z plane must be decomposed, as illustrated in Fig. (2-d), to resemble the geometry of the radial pole, thereby establishing a reluctance relationship for it.

Thus, the capacitances for sections 1 and 2 in y-z plane, can be computed by:

$$C_{1(y-z)} = \varepsilon_0 \left[\frac{D_{a2}}{4g} + \frac{2}{\pi} \left(1 + \ln \frac{\pi H_t}{4g} \right) \right]$$
 (13)

$$C_{2(y-z)} = \varepsilon_0 \left[\frac{D_{a2}}{4a} + \frac{2}{\pi} \left(1 + \ln \frac{\pi H_a}{4a} \right) \right]$$
 (14)

After some manipulations, the air gap reluctances in the two planes of axial poles, accounting for the fringing effect, are obtained as follows:

$$R_{a(y-z)} = \frac{1}{\mu_0 \left[\frac{D_{a2}}{2g} + \frac{4}{\pi} \left(1 + \ln \frac{\pi \sqrt{H_t \times H_a}}{4g} \right) \right]}$$
(15)

$$R_{a(x-y)} = \frac{1}{\mu_0 \left[\frac{D_{a1}}{g} + \frac{4}{\pi} \left(1 + \ln \frac{\pi H_a}{4g} \right) \right]}$$
(16)

According (15) and (16), 3D fringing factor for the air gap of the axial poles is equal to:

$$\sigma_{T} = \frac{\frac{1}{\mu_{0} \left[\frac{D_{a2}}{2g} + \frac{4}{\pi} \left(1 + \ln \frac{\pi \sqrt{H_{t} \times H_{a}}}{4g} \right) \right]}{\frac{g}{\mu_{0} D_{a2}}} \times \frac{1}{\mu_{0} \left[\frac{D_{a1}}{g} + \frac{4}{\pi} \left(1 + \ln \frac{\pi H_{a}}{4g} \right) \right]}{\frac{g}{\mu_{0} D_{a1}}}$$
(17)

Finally, the 3D inductances of radial poles in the displacement sensor can be computed by (18) and (19). Equations (18) and (19) can be also applied for $L_{r3-B} = L_{r4-B}$ and $L_{r1-B} = L_{r2-B}$, respectively. Moreover, since the

specific equation cannot be determined for 3D inductances of the axial poles (for instance La1 and La2), the air gap reluctances of four poles of the axial section are presented in (20) and (21).

IV. SIMULATION RESULTS

In this section, to investigate the accuracy of 3D inductance calculations, the results of this method are compared with those obtained from the FEM. For this purpose, the position sensor ring is simulated in the Ansys software using magnetostatic analysis. Figure 3 displays the flux density distribution in different parts of the sensor. To clarify the coupling between the windings, a high voltage is applied to them to increase the flux density. As observed, in the modeling of the radial section, the leakage flux between the poles of two radial axes A and B has been ignored due to the coupling coefficient close to one in both adjacent poles of one axis. Therefore, only two radial poles in one axis are selected to investigate the theoretical model, and the results are similar for other poles. Similarly, only four poles are used for axial calculations. The geometric dimensions of the radial and axial poles of the sensor are presented in Table 1. In Fig. 4, the selfinductances of the radial poles for various air gaps are depicted for three models, including (1) the ideal model (without considering the fringing effect), (2) the analytical model (taking the fringing effect into account), and (3) the FEM. As observed, the self-inductances of the radial windings decrease with the increase of air gap length. The error between the ideal model and the analytical model compared to the FEM is shown in Fig. 5. As observed, with an increase in the air gap, the flux fringing increases. Consequently, the error in the ideal model for an air gap variation of 0.8 mm increases by approximately 30%. Meanwhile, the analytical model, with a consistent 8% error, demonstrates better accuracy than the ideal model. In Figs 6 and 7, the self-inductances of the axial pole windings versus different axial displacements are depicted for air gaps of 0.4 mm and 0.8 mm. A zero displacement signifies a position where the rotor aligns precisely in the middle of all four axial poles and shares the same cross-sectional area with each. As the rotor moves in the positive Z direction, the self-inductance of winding La1-1 decreases while that of winding La2-1 increases, proportionally to the effective cross section. As observed, in the axial part, the analytical model exhibits an error of about 6.5% compared to the FEM, which is much more accurate than the ideal model, with an error of 65% compared to the FEM.

The errors between mutual inductances of axial poles obtained from the FEM and both the analytical and ideal models are shown in Fig. 8 for an air gap of 0.4 mm. According to this figure, in the negative axial displacement of 0.6, where the rotor with La1-1 and La1-2 has the largest effective cross section, both ideal and analytical models have the same accuracy. But as the rotor moves in the positive Z direction and the effective cross section decreases, the error of the ideal model increases so that in the positive displacement of 0.6, the error of the ideal model is about 3 times more than the analytical model. The results indicate that the analytical model can accurately simulate the 3D inductances of the sensor poles. By employing this method, it becomes possible to model the behavior of the sensor, which relies on changes in winding inductance.

Table 1. Parameters of Radial and axial geometries

| Parameter | Value | Parameter | Value | Parameter | Value |
|-----------|-------|-----------|-------|-----------|-------|
| Hr (mm) | 13.5 | Dr1 (mm) | 12.5 | Da2 (mm) | 3 |
| Ha1 (mm) | 12 | Dr2 (mm) | 5 | N | 50 |
| Ht (mm) | 10 | Da1 (mm) | 11.5 | | |

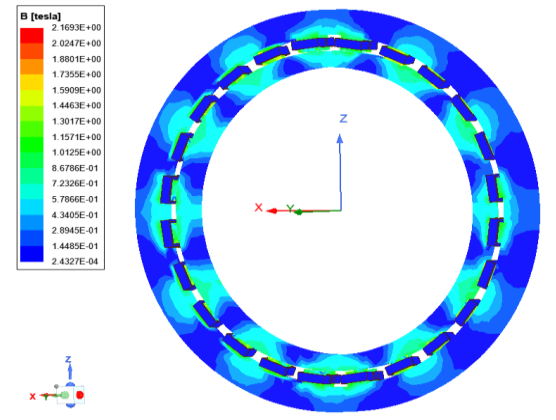


Fig. 3. The flux density distribution within the 3-DOF position sensor

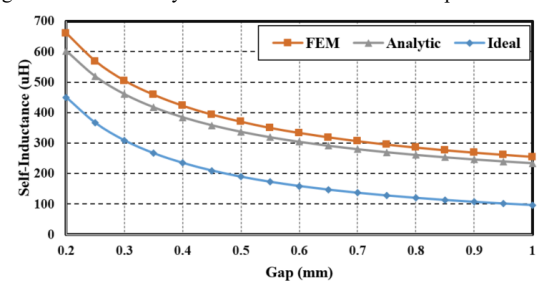


Fig. 4. The self-inductance of the radial windings

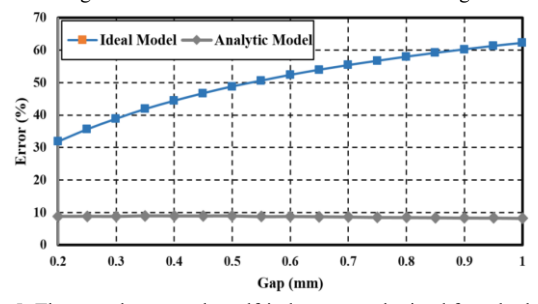


Fig. 5. The error between the self-inductances obtained from both the analytical and ideal models, as compared to those from the FEM.

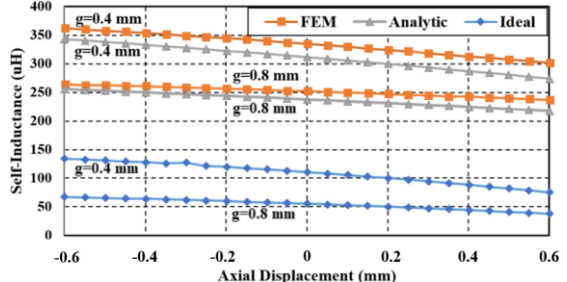


Fig. 6. The self-inductance of the axial winding La1-1

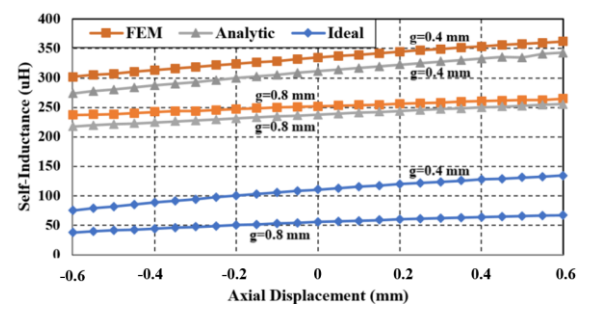


Fig. 7. The self-inductance of the axial winding La1-3

$$L_{r_{1-A}} = L_{r_{4-A}} = \frac{N^2 \mu_0 \left[D_{r_1} + \frac{4(g + \Delta y)}{\pi} \left(1 + \ln \frac{\pi H_r}{4(g + \Delta y)} \right) \right] \left[D_{r_2} + \frac{4(g + \Delta y)}{\pi} \left(1 + \ln \frac{\pi H_r}{4(g + \Delta y)} \right) \right]}{2(g + \Delta y)}$$
(18)

$$L_{r1-2} = L_{r3-A} = \frac{N^2 \mu_0 \left[D_{r1} + \frac{4(g - \Delta y)}{\pi} \left(1 + \ln \frac{\pi H_r}{4(g - \Delta y)} \right) \right] \left[D_{r2} + \frac{4(g - \Delta y)}{\pi} \left(1 + \ln \frac{\pi H_r}{4(g - \Delta y)} \right) \right]}{2(g - \Delta y)}$$
(19)

$$R_{1} = R_{2} = \frac{g}{\mu_{0} \left[D_{a1} + \frac{4g}{\pi} \left(1 + \ln \frac{\pi H_{a}}{4g} \right) \right] \left[\left(\frac{D_{a2} + \Delta z}{2} \right) + \frac{4g}{\pi} \left(1 + \ln \frac{\pi \sqrt{H_{t} \times H_{a}}}{4g} \right) \right]}$$

$$R_{2} = R_{4} = \frac{g}{\mu_{0} \left[D_{a1} + \frac{4g}{\pi} \left(1 + \ln \frac{\pi H_{a}}{4g} \right) \right]}$$
(20)

$$R_{3} = R_{4} = \frac{g}{\mu_{0} \left[D_{a1} + \frac{4g}{\pi} \left(1 + \ln \frac{\pi H_{a}}{4g} \right) \right] \left[\left(\frac{D_{a2} - \Delta z}{2} \right) + \frac{4g}{\pi} \left(1 + \ln \frac{\pi \sqrt{H_{t} \times H_{a}}}{4g} \right) \right]}$$
(21)

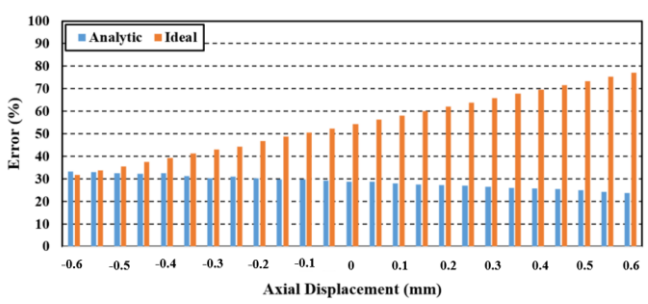


Fig. 8. The mutual inductance error between the windings La1-1 and La1-2

V. CONCLUSION

This study aimed to address the fringing effects in air gaps on the performance of inductive displacement sensors, particularly in the context of their application in the AMB systems. By utilizing a theoretical model to compute the matrix of inductances within the 3D geometry of a threedegree-of-freedom inductive sensor, the research sought to enhance the accuracy of sensor analysis. Comparison between theoretical model outcomes and finite element results highlighted the superior precision of the theoretical model relative to the idealized one. The investigation also underscored the significance of considering fringing effects, which are often overlooked in conventional analyses. Through the application of the Schwarz-Christoffel transformation, this study successfully accounted for these effects, enabling a more comprehensive evaluation of sensor behavior. The findings demonstrate the importance of incorporating fringing effects for accurate characterization, thereby advancing the understanding and optimization of inductive sensor systems for industrial applications.

ACKNOWLEDGMENT

The authors express their gratitude to Kavosh Electronic Vanda Shargh company for their support and provision of documents and technical reports concerning active magnetic bearings.

REFERENCES

[1] K. N. V. Prasad and G. Narayanan, "Electromagnetic Bearings With Power Electronic Control for High-Speed Rotating Machines: Review, Analysis, and Design Example," *IEEE Transactions on Industry Applications*, vol. 57, no. 5, pp. 4946-4957, Sept.-Oct. 2021.

- [2] M. Sun, J. Zhou, B. Dong, and S. Zheng, "Driver Circuit Improvement of Eddy Current Sensor in Displacement Measurement of High-Speed Rotor," *IEEE Sensors J.*, vol. 21, no. 6, pp. 7776–7783, Mar. 2021.
- [3] S. Fericean and R. Droxler, "New Noncontacting Inductive Analog Proximity and Inductive Linear Displacement Sensors for Industrial Automation," *IEEE Sensors J.*, vol. 7, no. 11, pp. 1538–1545, Nov. 2007.
- [4] Z. Ren, H. Li, X. Chen, W. Yu and R. Chen, "Impedance Modeling of Self-Inductive Displacement Sensor Considering Iron Core Reluctance and Flux Leakage," *IEEE Sensors Journal*, vol. 22, no. 9, pp. 8583-8595, 1 May1, 2022.
- [5] W. Li, J. Hu, Z. Su and D. Wang, "Radial Displacement Detection Using Sensing Coils Weakly Coupled with Magnetic Bearing," *IEEE Sensors Journal*, vol. 22, no. 21, pp. 20352-20359, 1 Nov.1, 2022.
- [6] Y. Wang, Y. Qin, X. Chen, Q. Tang, T. Zhang and L. Wu, "Absolute Inductive Angular Displacement Sensor for Position Detection of YRT Turntable Bearing," *IEEE Transactions on Industrial Electronics*, vol. 69, no. 10, pp. 10644-10655, Oct. 2022.
- [7] B. Xiang and T. Wen, "An Integrated 5-DoF Displacement Sensor System of Magnetically Suspended Flywheel," *IEEE Transactions on Instrumentation and Measurement*, vol. 72, pp. 1-11, 2023.
- [8] A. Babu and B. George, "Design and Development of a New Non-Contact Inductive Displacement Sensor," *IEEE Sensors Journal*, vol. 18, no. 3, pp. 976-984, Feb. 2018.
- [9] Y. Jiang, K. Wang, M. Sun and J. Xie, "Displacement Self-Sensing Method for AMB-Rotor Systems Using Current Ripple Demodulations Combined with PWM Command Signals," *IEEE Sensors Journal*, vol. 19, no. 14, pp. 5460-5469, July 2019.
- [10] Y. Li, R. Li, J. Yang, J. Xu, and X. Yu, "Effect of Excitation Signal on Double-Coil Inductive Displacement Transducer," *Sensors*, vol. 23, no, 7, pp. 1-17, Apr. 2023.
- [11] L. Wu, S. Xu, Z. Zhong, C. Mou, and X. Wang "An Inductive Sensor for Two-Dimensional Displacement Measurement," Sensors, vol. 20, no, 7, pp. 1-15, Mar. 2020.
- [12] C. Rui, L. Hongwei and T. Jing, "Structure Design and Simulation Analysis of Inductive Displacement Sensor," 13th IEEE Conference on Industrial Electronics and Applications (ICIEA), Wuhan, China, pp. 1620-1626, 2018.
- [13] K. Wang, L. Zhang, Y. Le, S. Zheng, B. Han and Y. Jiang, "Optimized Differential Self-Inductance Displacement Sensor for Magnetic Bearings: Design, Analysis and Experiment," *IEEE Sensors Journal*, vol. 17, no. 14, pp. 4378-4387, July 2017.
- [14] T. Sillanpää, A. Smirnov, P. Jaatinen, J. Vuojolainen, N. Nevaranta, R. Jastrzebski, and O. Pyrhönen, "Three-Axis Inductive Displacement Sensor Using Phase-Sensitive Digital Signal Processing for Industrial Magnetic Bearing Applications," *Actuators*, vol. 10, no. 6, pp. 1-16, May 2021.
- [15] S.-H. Yang, K. Hirata, T. Ota, Y. Mitsutake, and Y. Kawase, "Impedance Characteristics Analysis of the Non-Contact Magnetic Type Position Sensor," *Electronics and Communations in Japan*, vol. 94, no. 3, pp. 33–40, Mar. 2011.
- [16] J. Mühlethaler, J. W. Kolar, and A. Ecklebe, "A Novel Approach for 3D Air Gap Reluctance Calculations," 8th International Conference on Power Electronics The Shilla Jeju, Korea, 2011.
- [17] W. Li, J. Hu, Z. Su, D. Wang, "Analysis and Design of Axial Inductive Displacement Sensor," *Measurement*, vol. 187, pp. 1-8, Jan. 2022.